SUPER AWESOME MARATHON THESIS

A dissertation submitted

to Kent State University

in partial fulfillment of the requirements

for the degree of Doctor of Philosophy

by

Tyler Hague

December 2019

Dissertation written by

Tyler Hague

B.S., Abilene Christian University, 2012

Ph.D., Kent State University, TBD

Approved by

Gerassimos Petratos, Co-Chair, Doctoral Dissertation Committee

Assimoula Katramatou, Co-Chair, Doctoral Dissertation Committee

James Doe, Members, Doctoral Dissertation Committee

Julia Doe

Jeffrey Doe

Accepted by

James T. Gleeson, Chair, Department of Physics

James L. Blank, Dean, College of Arts and Sciences

TABLE OF CONTENTS

LIST OF FIGURES

LIST OF TABLES

CHAPTER 1

Electron Scattering and Nuclear Structure

1.1 History

Ernest Rutherford performed what is often considered the first scattering experiment. This experiment fired an α-particle beam at gold foil. The result of this experiment saw most particles pass through the foil completely undeflected. Those that did deflect were scattered at a large range of angles. This gave the world a new view of the nucleus, that of a largely empty space with a few hard scattering centers. We now know that these scattering centers are the nucleus of the atom, formed by a dense combination of protons and neutrons.[1]

Since this time, many experiments have been conducted that expanded our view of the nucleus. The evidence of quarks at SLAC once again revolutionized our understanding of the nucleus. In this experiment, electrons were scattered off protons over a large momentum transfer, q^2, and final hadronic invariant mass, W, range. This experiment noted a "surprisingly weak" q^2 dependence once the kinematics reached the $W > 2$GeV range, a key feature of Deep Inelastic Scattering.[2] In this view the nucleons, protons and neutrons, are comprised of quarks. These quarks are elementary particles that define the characteristics and structure of the nucleon.[3]

This discovery paved the way for a wave of Deep Inelastic Scattering experiments. These experiments have refined our understanding of the nucleus and its constituent components. Deep Inelastic Scattering has proven to be a one of the most powerful tools available when one seeks to study nuclear structure.

1.2 Electron Scattering

Electron scattering allows for finely tuned analysis of the nucleus. By manipulating the energy of the incoming electron and the kinematic variables accepted by the detectors used, experimenters can choose what aspect of the nucleus will be probed. This technique has been used to study the structure of the nucleus all the way down to the properties of the constituent quarks.

There are four kinematic regimes of electron scattering that can be explored: elastic, quasi-elastic, resonance, and deep inelastic scattering. Each of these regimes are defined by the kinematics and the underlying physical structure that they are sensitive to.

Elastic scattering occurs when the electron scatters coherently off of the nucleus. This occurs at low momentum and energy transfer. At these kinematics, the electron is sensitive to the size of the nucleus. The size of the nucleus is accessed by extracting nuclear "form factors" from the measured cross sections. From this we can learn about the charge distributions, magnetic moments, and charge radius of the nucleus.

Quasi-elastic scattering occurs at larger energy transfers when the electron scatters elastically off of the nucleon, rather than the nucleus. At these kinematics, the electron is sensitive to the form factors of the nucleon.

Resonance scattering occurs at even larger momentum and energy transfers. In this region, some of the energy is used to excite the nucleon into a higher energy state, called a resonance. A resonance is a short-lived particle. The resonance will quickly decay back into the nucleon and emit the excess energy as an additional particle. For example, $ep \rightarrow e\Delta^+ \rightarrow ep\pi^0$.

As we push the momentum and energy transfer further, we enter the Deep Inelastic Scattering (DIS) region. As Q^2 is increased into the transition region between resonance and DIS, the resonance peaks begin to smooth out. Here the electron becomes sensitive to the constituent parts of the nucleon. The wavelength of the exchanged photon is inversely proportional to Q^2. DIS scattering is of particular interest because the wavelength is sufficiently small enough to discern the parton structure. Through careful measurement, we can access the nuclear structure functions and the parton distributions in the the nucleons.[4–6]

The MARATHON experiment seeks to study the nuclear and nucleon structure functions, as well as nucleon parton distributions. The kinematics used are in the DIS region in order to facilitate this study. The remainder of this chapter will be focused on the DIS cross section and what we can learn from it.

1.2.1 Deep Inelastic Scattering Cross Section

Deep Inelastic Scattering, shown in Figure 1, involves a high energy electron scattering off of a nucleon. In the lowest order perturbation, a virtual photon is exchanged between the electron and

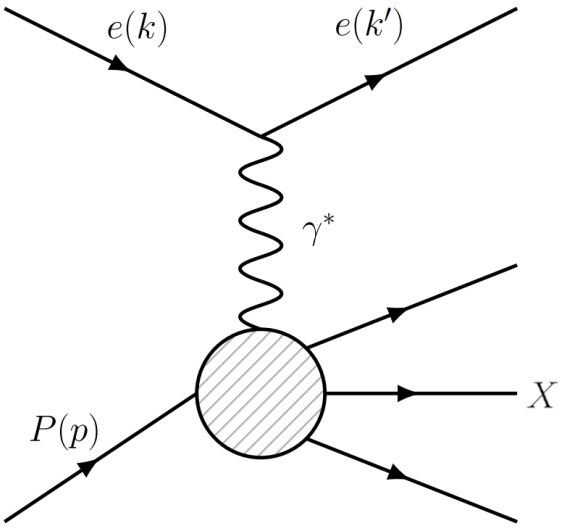

Figure 1: Feynman Diagram of Deep Inelastic Scattering

nucleon. This momentum transfer then excites the nucleon into a hadronic final state. Though the final hadronic state is undetected, the detection of the scattered electron can yield insight into the interaction.

The reaction, for scattering off a proton, is written as:

$$e^- + P \to e^- + X$$

In this section, there will be many variables defined. For clarity, the meaning of these variable are defined in Table 1. Mathematical definitions will follow as necessary.

The kinematics of scattering are typically defined by he Lorentz-invariant kinematic variables Q^2 and W^2, as well as the energy difference ν. These variables are defined as:

$$q^2 \equiv -Q^2 = \left(k - k'\right)^2 \tag{1.1}$$

$$W^2 = (p+q)^2 \tag{1.2}$$

$$\nu = E - E' \tag{1.3}$$

Q^2	Negative of the 4-momentum transfer
W^2	Square of the invariant mass of the final hadronic state
E	Beam energy
E'	Scattered electron energy
$L_{\mu\nu}$	Electron tensor
$W^{\mu\nu}$	Symmetric hadronic tensor
k	4-momentum of the incident electron
k'	4-momentum of the scattered electron
p	4-momentum of the target nucleon
θ	Scattered electron angle
ν	Energy difference between incoming and scattered electron
M	Proton mass
m	Electron mass

Table 1: Variable definitions introduced in this section

Now it is useful to analyze in the laboratory rest frame and to note that MARATHON is a fixed target experiment. In this frame, the target is "at rest" (i.e. having a four-momentum of $(M, 0)$). This leads to a simplification of Q^2 and W^2.

$$Q^2 = 4EE' \sin^2 \frac{\theta}{2} \tag{1.4}$$

$$W^2 = M^2 + 2M\nu - Q^2 \tag{1.5}$$

Electron-nucleon scattering can be generally expressed as the following:

$$\frac{d^2\sigma}{d\Omega dE'} = \frac{\alpha^2}{Q^4} \frac{E'}{E} L_{\mu\nu} W^{\mu\nu} \tag{1.6}$$

The electron tensor is expressed as:

$$L_{\mu\nu} = 2\left(k'^{\mu}k^{\nu} + k'^{\nu}k^{\mu} - \left(k' \cdot k - m^2\right) g^{\mu\nu}\right) \tag{1.7}$$

The DIS hadronic tensor is expressed in terms of structure functions W_1 and W_2:

$$W^{\mu\nu} = W_1 \left(-g^{\mu\nu} + \frac{q^\mu q^\nu}{q^2} \right) + \frac{W_2}{M^2} \left(p^\mu - \frac{p \cdot q}{q^2} q^\mu \right) \left(p^\nu - \frac{p \cdot q}{q^2} q^\nu \right) \tag{1.8}$$

Combining all of this, we arrive at the *ep* DIS cross section in the laboratory frame:

$$\left. \frac{d^2\sigma}{d\Omega dE'} \right|_{\text{lab}} = \frac{\alpha^2}{4E^2 \sin^4 \frac{\theta}{2}} \left[W_2 \cos^2 \frac{\theta}{2} + 2W_1 \sin^2 \frac{\theta}{2} \right] \tag{1.9}$$

1.3 Bjorken Scaling

As Q^2 is pushed higher, inelastic scattering begins to give way to DIS. In this kinematic region, the wavelength of the virtual photon is sufficiently short to resolve the internal structure of the nucleon. This transition sees the system begin to behave like a free Dirac particle, the parton. As the Bjorken limit is approached, $Q^2 \to \infty$ and $\nu \to \infty$, the scattering center approaches a structureless parton.[7] With this in mind, it is useful to look at the cross section for scattering off of a structureless target:

$$\frac{d^2\sigma}{d\Omega dE'} = \frac{\alpha^2}{4E^2 \sin^4 \frac{\theta}{2}} \left[\cos^2 \frac{\theta}{2} + \frac{Q^2}{2m^2} \sin^2 \frac{\theta}{2} \right] \delta \left(\nu - \frac{Q^2}{2M} \right) \tag{1.10}$$

Noting that DIS is scattering off of a structureless parton, we can compare (1.9) and (1.10). By equating these two cross sections, we can clearly extract equations for the DIS structure functions.

$$2MW_1 \left(Q^2, \nu \right) = \frac{Q^2}{2M\nu} \delta \left(1 - \frac{Q^2}{2M\nu} \right) \tag{1.11a}$$

$$\nu W_2 \left(Q^2, \nu \right) = \delta \left(1 - \frac{Q^2}{2M\nu} \right) \tag{1.11b}$$

In this kinematic region, we see that the structure functions are dependent on the ratio $\frac{Q^2}{2M\nu}$ rather than Q^2 and ν independently while the target mass sets the scale. Noting this dependency, the scaling variable Bjorken x is defined as

$$x = \frac{Q^2}{2M\nu}. \tag{1.12}$$

As the Bjorken limit is approached DIS is only dependent on x, showing little to no scaling with Q^2 or ν.[8] New structure functions, F_1 and F_2, are also defined in terms of x to clearly show the lack of scaling with Q^2 and ν independently:

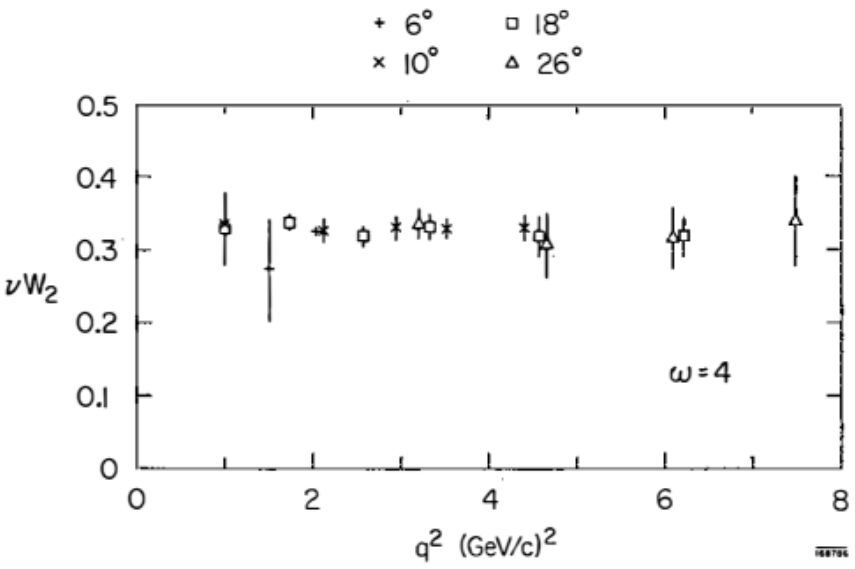

Figure 2: Proton data showing no Q^2 dependence of $\nu W_2 = F_2$ in the DIS region.[9]

$$2MW_1\left(Q^2,\nu\right) \to F_1\left(x\right) \tag{1.13a}$$

$$\nu W_2\left(Q^2,\nu\right) \to F_2\left(x\right) \tag{1.13b}$$

The independence of structure functions with respect to Q^2 has been experimentally tested. The data was taken at fixed x with varying Q^2. All measurements were consistent with no Q^2 dependence. Proton data showing this effect for the structure function F_2 can be seen in Figure 2. Substituting Equations 1.13 into Equation 1.9 we find the cross section in terms of DIS x, Equation 1.14.

$$\frac{d^2\sigma}{d\Omega dE'} = \frac{4\alpha^2\left(E'\right)^2}{Q^4}\cos^2\left(\frac{\theta}{2}\right)\left[\frac{F_2\left(x\right)}{\nu} + \frac{2F_1\left(x\right)}{M}\tan^2\left(\frac{\theta}{2}\right)\right] \tag{1.14}$$

1.4 Nuclear Structure Functions and The Quark Parton Model

Having shown that the nucleons consist of structureless partons we can define physics quantities in terms of the Quark-Parton Model (QPM). The QPM defines kinematic properties of the quarks and the nucleon structure functions in terms of constituent quark properties in the Bjorken limit.

In this regime, Bjorken x is the fraction of the momentum and energy contained by the parton scattered off of. To access the kinematics of the parton, we simply multiply the energy, momentum, and mass of the nucleon by x.

To analyze the structure functions of the nucleon, we first look at elastic scattering off of a parton. In this setup, we imagine that we have the means to determine what parton type the electron was scattered from. This is the same equation as Equation 1.10, but with α multiplied by the charge of the parton being scattered from, e_i, and replacing M with xM for the mass of the parton.

$$\frac{d^2\sigma}{d\Omega dE'} = \frac{\alpha^2 e_i^2}{4E^2 \sin^4 \frac{\theta}{2}} \left[\cos^2 \frac{\theta}{2} + \frac{Q^2}{2x^2M^2} \sin^2 \frac{\theta}{2}\right] \delta\left(\nu - \frac{Q^2}{2xM}\right) \tag{1.15}$$

Comparing this with the nuclear inelastic cross section, it is clear that the nuclear structure functions can be written in terms of parton structure functions. The parton structure functions can be derived using the same method as the nuclear structure functions.

$$W_1^i = \frac{e_i^2 Q^2}{4M^2x^2\nu} \delta\left(1 - \frac{Q^2}{2Mx\nu}\right) \tag{1.16a}$$

$$W_2^i = \frac{e_i^2}{\nu} \delta\left(1 - \frac{Q^2}{2Mx\nu}\right) \tag{1.16b}$$

Defining $f_i(x)$ as the probability that a parton i has the momentum fraction x, or parton distribution, we can then write the nucleon structure functions in terms of the parton structure functions. The delta function makes the integrals trivial.

$$W_1\left(Q^2, \nu\right) = \sum_i \int_0^1 \frac{e_i^2 Q^2}{4M^2x^2\nu} f_i(x)\, \delta\left(1 - \frac{Q^2}{2Mx\nu}\right) dx = \sum_i \frac{e_i^2}{2M} f_i(x) \tag{1.17a}$$

$$W_2\left(Q^2, \nu\right) = \sum_i \int_0^1 \frac{e_i^2}{\nu} f_i(x)\, \delta\left(1 - \frac{Q^2}{2Mx\nu}\right) dx = \sum_i \frac{e_i^2}{\nu} f_i(x) \tag{1.17b}$$

Using the definitions of the F structure functions in the previous sections, this formalism allows us to write them in terms of parton quantities.

$$MW_1\left(Q^2, \nu\right) = \sum_i \frac{e_i^2}{2} f_i(x) \equiv F_1(x) \tag{1.18a}$$

$$\nu W_2\left(Q^2, \nu\right) = \sum_i e_i^2 x f_i(x) \equiv F_2(x) \tag{1.18b}$$

These equations lead to a relation between the structure functions (in the Bjorken limit) called the Callan-Gross relation:

$$F_2(x) = 2xF_1(x) \tag{1.19}$$

Deriving the structure functions in terms of parton quantities also allows us to place constraints on the ratio of F_2 for the nucleons. Due to mass constraints, we can restrict this analysis to up ($q = 2/3$), down ($q = -1/3$), and strange ($q = -1/3$) quarks. Since the proton and neutron, along with the up and down quarks, form an isospin doublet we can relate their quark distributions (and extend this to their antiquark distributions):

$$u^p(x) = d^n(x) \equiv u \tag{1.20a}$$

$$d^p(x) = u^n(x) \equiv d \tag{1.20b}$$

$$s^p(x) = s^n(x) \equiv s \tag{1.20c}$$

Using these relations, we can write the nucleon structure functions and their ratio as:

$$F_2^p = x\left[\frac{4}{9}(u+\bar{u}) + \frac{1}{9}\left(d+\bar{d}\right) + \frac{1}{9}(s+\bar{s})\right] \tag{1.21a}$$

$$F_2^n = x\left[\frac{4}{9}\left(d+\bar{d}\right) + \frac{1}{9}(u+\bar{u}) + \frac{1}{9}(s+\bar{s})\right] \tag{1.21b}$$

$$\frac{F_2^n}{F_2^p} = \frac{[(u+\bar{u}) + (s+\bar{s})] + 4\left(d+\bar{d}\right)}{\left[\left(d+\bar{d}\right) + (s+\bar{s})\right] + 4(u+\bar{u})} \tag{1.22}$$

This equation can be evaluated noting that by definition quark distributions must be positive. This naturally leads to a constraint on F_2^n/F_2^p known as the Nachtmann inequality:

$$\frac{1}{4} \leq \frac{F_2^n}{F_2^p} \leq 4 \tag{1.23}$$

1.5 $R = \sigma_L/\sigma_T$

If we instead approach DIS as the production and absorption of a virtual photon by a parton we can extract a different structure function $R = \sigma_L/\sigma_T$, referred to as photonuclear R. That is, the ratio of the cross sections for absorbing longitudinal photons, σ_L, to transverse photons, σ_T. In

the Bjorken limit, as in the previous section, $R \to 0$. In practice the Bjorken limit is an imperfect approximation and it is useful to consider the effects of large, but finite, Q^2 and ν.

We can write the DIS cross section in terms of these cross sections as

$$\frac{d^2\sigma}{d\Omega dE'}\left(E, E', \theta\right) = \Gamma\left[\sigma_T\left(x, Q^2\right) + \epsilon\sigma_L\left(x, Q^2\right)\right]. \tag{1.24}$$

In this equation Γ is the flux of transverse virtual photons and ϵ is the relative flux of longitudinal virtual photons. These are defined by

$$\Gamma = \frac{\alpha K E'}{2\pi^2 Q^2 E_0 \left(1-\epsilon\right)} \tag{1.25}$$

and

$$\epsilon = \frac{1}{1 + 2\left(1 + \nu^2/Q^2\right)\tan^2\left(\frac{\theta}{2}\right)}. \tag{1.26}$$

Here, K is the laboratory photon energy,

$$K = \frac{W^2 - M^2}{2M}. \tag{1.27}$$

By comparing these equations to Equation 1.14 F_1 and F_2 can be related to σ_L, σ_T, and each other.

$$\sigma_T = \frac{4\pi\alpha^2}{KM} F_1 \tag{1.28}$$

$$\sigma_L = \frac{4\pi\alpha^2}{KM}\frac{1}{2x}\left[F_2 - 2xF_1\right] \tag{1.29}$$

$$F_1 = \frac{F_2\left(1 + Q^2/\nu^2\right)}{2x\left(1+R\right)} \tag{1.30}$$

Substituting this into our DIS cross section equation, we can eliminate F_1. This also makes it clear that we can easily access the F_2 structure functions by measuring cross section ratios.

$$\frac{d^2\sigma}{d\Omega dE'}\left(E, E', \theta\right) = \frac{4\alpha^2\left(E'\right)}{Q^4}\cos^2\left(\frac{\theta}{2}\right) F_2\left[\frac{1}{\nu} + \frac{\left(1 + Q^2/\nu^2\right)}{xM\left(1+R\right)}\tan^2\left(\frac{\theta}{2}\right)\right] \tag{1.31}$$

If we measure the cross section ratios of two different targets at the same kinematics (that is the same x, E, E', and θ) we find:

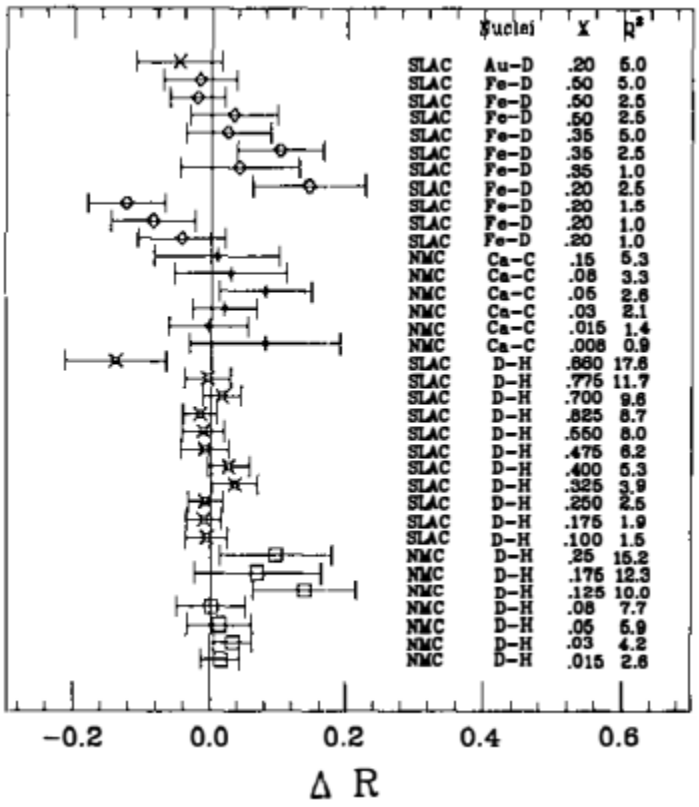

Figure 3: Historical data of $R = \sigma_L/\sigma_T$. This data shows measurements of the difference in R between two nuclei. The data is consistent with no nuclear dependence.[10]

$$\frac{\sigma_A}{\sigma_B} = \frac{F_2^A}{F_2^B} \frac{\left[\frac{1}{\nu} + \frac{\left(1+Q^2/\nu^2\right)}{xM(1+R^A)} \tan^2\left(\frac{\theta}{2}\right)\right]}{\left[\frac{1}{\nu} + \frac{(1+Q^2/\nu^2)}{xM(1+R^B)} \tan^2\left(\frac{\theta}{2}\right)\right]} \tag{1.32}$$

As shown in Figure 3, historical data suggests that photonuclear R has no nuclear dependence to within 10%. If we assume that that there is no nuclear dependence, this equation simplifies to:

$$\frac{\sigma_A}{\sigma_B} = \frac{F_2^A}{F_2^B} \tag{1.33}$$

By measuring the cross section ratios of targets in the DIS region, we can easily access the nuclear structure functions of the targets.

1.6 F_2^n/F_2^p

The structure functions of the nucleons are common inputs to models. Making use of a Hydrogen target the F_2^p structure function is easily accessible. Unfortunately, there is no free neutron target. This absence means that there is no way to direct way to measure F_2^n. However, with the proper input, we can extract the ratio F_2^n/F_2^p.

To extract this ratio, we first define "EMC-type" ratios. These are simply the ratio of the nuclear structure function to the sum of its constituent nucleons. The "EMC-type" ratios for ^{3}He and ^{2}H are:

$$R_{\mathrm{EMC}}\left(^3\mathrm{He}\right) = \frac{F_2^{^3\mathrm{He}}}{2F_2^p + F_2^n} \tag{1.34}$$

$$R_{\mathrm{EMC}}\left(^2\mathrm{H}\right) = \frac{F_2^{^2\mathrm{H}}}{F_2^p + F_2^n} \tag{1.35}$$

These can be used to create a "Super-Ratio", $\mathcal{R}$, as the ratio of "EMC-type" ratios.

$$\mathcal{R} = \frac{R_{\mathrm{EMC}}\left(^3\mathrm{He}\right)}{R_{\mathrm{EMC}}\left(^2\mathrm{H}\right)} = \frac{F_2^{^3\mathrm{He}}}{2F_2^p + F_2^n} \cdot \frac{F_2^p + F_2^n}{F_2^{^2\mathrm{H}}} \tag{1.36}$$

Solving this for F_2^n/F_2^p makes it clear that the quantity can be easily extracted with a cross section ratio measurement and a model input for $\mathcal{R}$.

$$\frac{F_2^n}{F_2^p} = \frac{F_2^{^3\mathrm{He}}/F_2^{^2\mathrm{H}} - 2\mathcal{R}}{\mathcal{R} - F_2^{^3\mathrm{He}}/F_2^{^2\mathrm{H}}} \tag{1.37}$$

CHAPTER 2

The EMC Effect

2.1 History

The EMC effect was first discovered by its namesake the European Muon Collaboration (EMC group) in 1983. The EMC group measured the structure functions of hydrogen, deuterium, and iron. After correcting for the neutron excess, the per nucleon F_2 structure function ratio of iron to deuterium was calculated, as seen in Figure 4. This data showed a clear x dependence, contrary to expectations.

Prior to this original measurement, nucleons were assumed to be quasi-free within the nucleus. In this understanding the nuclear F_2 structure function would be described as

$$F_2^A = Z F_2^p + (A - Z) F_2^n. \tag{2.1}$$

This description leads to the prediction that the per nucleon structure function ratio of any two isoscalar targets will be unity. At this time, the only other expected nuclear effect was Fermi motion. Fermi motion causes a sharp rise in the per nucleon structure function ratio at high x, but would leave the ratio largely unchanged at low x.

The original experiment did not originally set out to measure the EMC effect, rather the data was a byproduct of efforts to achieve higher luminosity. Because of this, the data had very large uncertainty on the measurement. However, the uncertainties were small enough that the anomaly could be confirmed.

Shortly after the original EMC measurement a Rochester-SLAC-MIT group analyzed previous SLAC data to confirm the phenomenon. The data analyzed not only confirmed the effect in iron, but also in aluminum. The iron data showed the EMC effect as well as the expected rise from Fermi motion at high x. The aluminum data showed these phenomena as well as low x shadowing and anti-shadowing. [12–14]

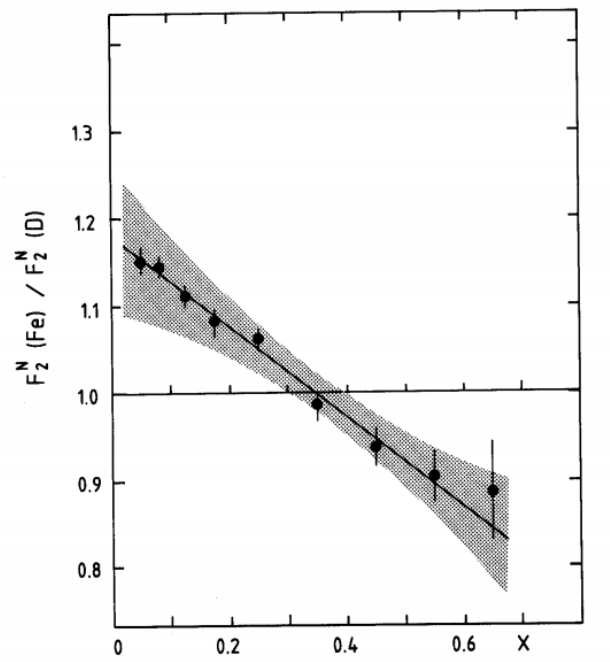

Figure 4: Results from the EMC collaboration showing a clear x dependence of the per-nucleon F_2 structure function ratio[11]

2.2 Further Results

Since that time, numerous experiments have measured nuclear F_2 structure function data in order to better understand the nature of this anomaly. These searches have primarily focused on heavy isoscalar nuclei. The following represents a non-exhaustive presentation of these experiments.

2.2.1 SLAC

At SLAC a new experiment was set up with the explicit goal of measuring the EMC effect in a wide range of nuclei. The data cover a large kinematic range of $0.089 \leq x \leq 0.8$ and $2\,(\mathrm{GeV/c})^2 \leq Q^2 \leq 15\,(\mathrm{GeV/c})^2$. This data confirms the phenomenon seen by the EMC group in the $x > 0.3$ region, but also sees a downturn in the ratios at low x.

The targets studied were ^{4}He, Be, C, Al, Ca, Fe, Ag, and Au. These results are shown in Figure 5. This target range allowed them to study the mass number A-dependence of the EMC effect. This data suggests an approximately $\ln(A)$ dependence on the strength of the EMC effect, with notable outliers of ^{4}He and Be. [15, 16]

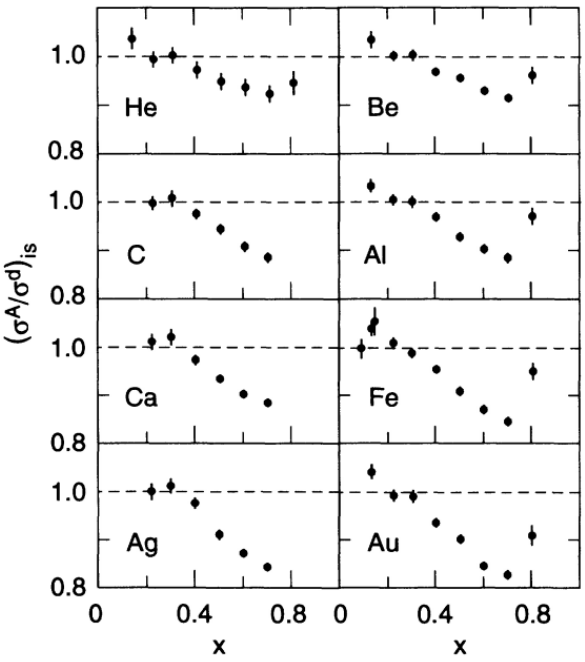

Figure 5: Results from SLAC showing an A-dependent EMC effect[16]

2.2.2 BCDMS

The BCDMS experiment at CERN measured the N and Fe EMC ratios. The iron data is consistent with the original EMC measurement within a normalization discrepancy. The nitrogen data is consistent with the SLAC carbon data. The BCDMS results show no Q^2 dependence in the EMC effect. However, BCDMS does not demonstrate an A-dependence of the EMC effect as SLAC did.[14]

2.2.3 EMC

The EMC group performed three more experiments to study the EMC effect.

The first of these experiments set out to improve the systematics of the original experiment. This followup measured the EMC ratio of C, Cu, and Sn. This data agrees with the original data for $x \geq 0.08$. However, below this threshold the data sees a downturn, the shadowing region, that the original experiment did not see.[17]

The NA28 experiment focused on studying the EMC ratio of C and Ca at low x. This data confirms the shadowing effect seen in the previous EMC data, the ratio drops below unity in the

region of $x < 0.1$. These results also shows that the shadowing region has no Q^2 dependence. The data overlaps well with previous measurements.

The last EMC group experiment to study the EMC effect remeasured the copper EMC ratio. To minimize systematics two 1m ^{2}H targets and three Cu targets were used. These results agree with the results from the first followup and are of greater precision.

2.2.4 NMC

The New Muon Collaboration (NMC) continued the study of the EMC effect at CERN. Initially NMC measure the EMC ratio of Li, C, and Ca to high precision at low x. This data was taken with two goals: to confirm the EMC data in the shadowing region and to study the effect of nuclear size and density on the EMC ratio. The data confirms the previous EMC measurement and found a very weak Q^2 dependence. Lithium and carbon have approximately the same size nucleus, but different nuclear densities. Calcium and carbon have the approximately the same nuclear density, but calcium has a bigger nucleus. It was found that both of these factors play a part in the suppression of the EMC ratio in the shadowing region. Increases in nuclear size or density show an increase in the suppression of the EMC ratio due to nuclear shadowing.

NMC then set out to study the difference between the photonuclear R of different targets in the region of $0.01 \leq x \leq 0.3$. The results were found, within uncertainties, to be compatible with zero. This result confirms that $\sigma_A/\sigma_D = F_2^A/F_2^D$.

Finally, the NMC group studied the EMC effect on Be, C, Al, Ca, Fe, Sn, and Pb. These results again confirm that there is no Q^2 dependence of the EMC ratio above $x = 0.06$. These data agree with the SLAC result finding that the EMC effect is approximately logarithmic with A.[18]

2.2.5 HERMES

The HERMES experiment ran at the HERA collider. This experiment collided positrons with protons to study the EMC effect on ^{3}He and N. Data was taken for $0.013 \leq x \leq 0.65$ and $0.5\,(\mathrm{GeV/c})^2 \leq Q^2 \leq 15\,(\mathrm{GeV/c})^2$. In the $x < 0.06$ region, the HERMES results differed drastically from the NMC results. Initially this was misreported as an A dependence of photonuclear R. This reporting was later amended when it was found that the difference could be attributed to a previously unaccounted for systematic effect.

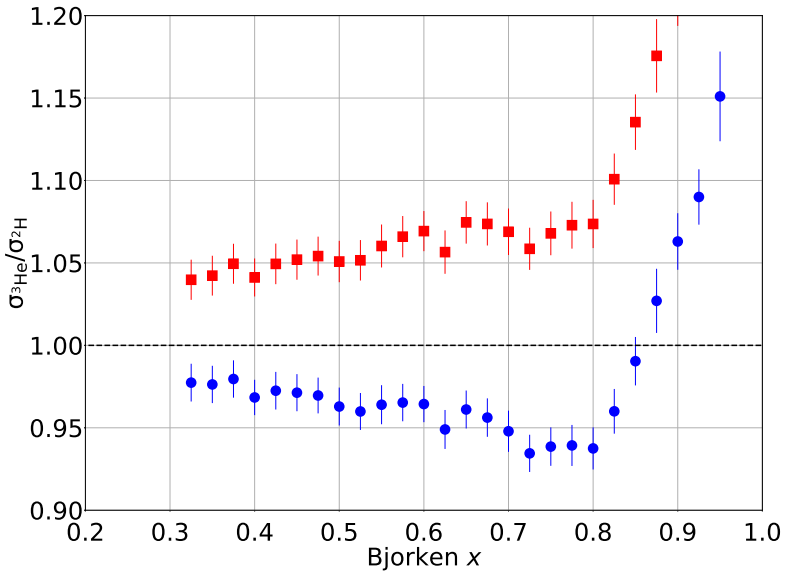

Figure 6: Helium-3 results from JLab E03-103. The upper red squares are the raw ratio and the lower blue circles have an isoscalar correction applied.[19]

2.2.6 JLab

The E03-103 experiment ran in Hall C at Jefferson Lab. This experiment studied the EMC effect in ^{3}He, ^{4}He, Be, and C. The kinematics covered were $0.3 < x < 0.9$ and $3\,(\mathrm{GeV/c})^2 < Q^2 < 6\,(\mathrm{GeV/c})^2$. The data measured was not purely DIS, but also included data in the resonance region. This led the experiment to extensively verify that their data was indeed independent of Q^2. The data for Beryllium is noted not to match the previous SLAC data. This is caused by the use of a different isoscalar correction and is further rectified by noting normalization uncertainties. These data show a significantly larger EMC effect in Beryllium than expected by the $\ln(A)$ prediction, which is consistent with SLAC noting that Beryllium is an outlier. The suggested explanation is that the EMC effect is dependent on *local* nuclear density rather than mean nuclear density. The ^{3}He results are showing in Figure 6.[19]

2.3 Structure Regions

In DIS F_2 structure function data, there are four phenomenological regions. In each region, different physics dominates the shape of the structure function ratio. Each kinematic region provides is a test bed for our understanding of nuclear physics. Studying these nuclear effects is the driving force

behind many experiments.[20, 21]

2.3.1 Shadowing

Nuclear shadowing is a phenomenon that occurs in the region of $x < 0.1$. Here, there is a depletion of the structure function when compared to deuterium. This depletion increases with mass number A. This depletion is also weakly dependent on Q^2 and mass number A. This effect is typically explained in terms of nuclear scattering which can be further investigated in reference [22].

2.3.2 Anti-shadowing

The Anti-shadowing, or enhancement, region is from $0.1 \leq x \leq 0.3$. In this region, the EMC structure function ratios are enhanced to greater than 1. Within experimental uncertainties, there is no Q^2 dependence in the anti-shadowing region.

2.3.3 EMC Effect

The EMC Effect region spans from $0.3 \leq x \leq 0.8$. In this kinematic area, the EMC structure function ratio falls off and reaches a minimum around $x = 0.65$. Since the discovery of the effect by the European Muon Collaboration, extensive EMC Effect region data has been recorded over a large Q^2 range. The data suggests that the EMC Effect is largely independent of Q^2. The EMC Effect does appear to be logarithmically dependent on mass number A.

2.3.4 Fermi Motion

As x is pushed past 0.8 the EMC structure function ratio sharply increases far beyond unity. In this region it is known that F_2^N, the free nucleon structure function, to drop as $(1-x)^3$. Fermi motion increases the structure function of the bound nucleon, causing the ratio to show this sharp increase.

2.4 Theories

There are many theories as to the origin of the EMC effect. To cover them all is beyond the scope of this thesis. This section will discuss the broad classes of models which can be investigated further in [10, 14, 23].

There are two primary groups of theories. Nuclear Structure focuses on the physics of scattering from a nucleus. Nucleon modification focuses on changes to quark momenta due to confinement effects.

2.4.1 Nuclear Structure

Nucleon Models

Traditional scattering calculations assume that the scattered nucleon was on-shell. This class of models gives the struck nucleon a negative average energy $\langle\epsilon\rangle$. This energy shift causes a rescaling of the x. This rescaling can explain the EMC effect region and Fermi motion. However, it is not capable of reproducing the anti-shadowing region.

Pion Enhancement

An enhancement of the nuclear pion field by nucleon-nucleon interactions. In these models the pion contribution is concentrated to low x. The creation of pions also requires the creation of Δ resonances in the nucleus.

Alone, this class of model has several problems. To reproduce high x data requires the presence of significantly more Δs than calculations suggest are plausible. In addition to this, matching anti-shadowing data causes a mismatch in high x data.

2.4.2 Nucleon Modification

Quark Bags

In quark cluster models quarks are confined to "bags" as defined by the MIT bag model. This creates color-singlet states with multiples of 3 quarks. The most common quark bag models rely on 6-quark bags. 6-quark bags are larger than a nucleon and thus lead to partial deconfinement of the quarks. This increase in confinement size leads to a decrease in quark momenta due to the uncertainty principle. A decrease in quark momenta in this way will suppress the structure function in the EMC region, leading to the EMC effect. [14, 23]

This quark bag model alone can compute many nuclear affects. It is hampered by the need for an additional free parameter to compute each new observable. This model has fallen out of favor due to failed predictions in the nuclear Drell-Yan process. [23]

Mean Field Enhancement

Mean Field Enhancement suggests that the structure functions of the nucleons are modified by nucleus surrounding them. Nucleons confined within the nucleus exchange mesons between the quarks of other confined nucleons. This modifies the nucleons structure to change the size of the quark confinement. The predicted increase in confinement size yields a smaller quark momentum.

[23, 24]

Short Range Correlations

Short Range Correlations (SRCs) greatly modify a few nucleons, rather than the small modification to all nucleons in mean-field enhancement. SRCs are the idea that there is a probability that two nucleon wavefunctions will overlap. In this scenario the overlapping wavefunctions will cause the size of quark confinement to greatly increase, drastically decreasing the quark momenta.

SRCs also predict an observed high momentum tail at $x > 1$. Studies of this effect have noted a correlation between the SRC "scale factor" and the strength of the EMC effect, the slope of the EMC ratio in the EMC region. [23, 25, 26]

Discerning between Mean Field Enhancement and SRCs

Both Mean Field Enhancement and SRCs have been shown to have accurate predictive power within the datasets available. This leads to the conundrum of finding an unmeasured quantity for which the two models make different predictions. Hen [23] and Thomas [27] discuss that mean field theory and SRCs make seemingly contradictory predictions for the polarized EMC effect. Mean field theory predicts that polarization will enhance the effect; SRCs predict the polarization to minimize the effect. This will be tested in Jefferson Lab Hall C by measuring the spin structure functions of ^{7}Li [28].

Bibliography

[1] D. Griffiths, *Introduction to Elementary Particles*, 2nd, WILEY-VCH, **2012**.

[2] E. D. Bloom, D. H. Coward, et al., *Physical Review Letters* **1969**, *23*, 930–934.

[3] E. M. Riordan, *Science* **1992**, *256*, 1287–1293.

[4] E. M. Henley, A. Garcia, *Particles and Nuclei*, Springer, **2008**.

[5] B. Povh, K. Rith, et al., *Particles and Nuclei: An Introduction to the Physical Concepts*, Second, Springer.

[6] W. E. Burcham, M Jobes, *Nuclear and Particle Physics*, Longman Scientific & Technical.

[7] J. D. Bjorken, *Physical Review* **1969**, DOI 10.1103/PhysRev.179.1547.

[8] A. Bodek, M. Breidenbach, et al., *Physical Review D* **1979**, DOI 10.1103/PhysRevD.20.1471.

[9] J. I. Friedman, H. W. Kendall, *Annual Review of Nuclear Science* **1972**, *22*, 203–254.

[10] D. Geesaman, K. Saito, et al., *Annual Review of Nuclear and Particle Science* **1995**, DOI 10.1146/annurev.nucl.45.1.337.

[11] J. J. Aubert, G. Bassompierre, et al., *Physics Letters B* **1983**, *123*, 275–278.

[12] A. Bodek, N. Giokaris, et al., *Physical Review Letters* **1983**, *50*, 1431–1434.

[13] A. Bodek, N. Giokaris, et al., *Physical Review Letters* **1983**, DOI 10.1103/PhysRevLett.51.534.

[14] P. R. Norton, *Rep. Prog. Phys.* **2003**, *66*, 1253–1297.

[15] R. G. Arnold, P. E. Bosted, et al., *Physical Review Letters* **1984**, DOI 10.1103/PhysRevLett.52.727.

[16] J. Gomez, R. G. Arnold, et al., *Physical Review D* **1994**, *49*, 4348–4372.

[17] J. Ashman, B. Badelek, et al., *Physics Letters B* **1988**, DOI 10.1016/0370-2693(88)91872-2.

[18] M. Arneodo, A. Arvidson, et al., *Nuclear Physics B* **1996**, *481*, 3–22.

[19] J Seely, A Daniel, et al., 1–5.

[20] G. Piller, W. Weise, *Physics Report* **2000**, *330*, 1–94.

[21] G. I. Smirnov, *European Physical Journal C* **1999**, *10*, 239–247.

[22] N. Armesto, *Journal of Physics G: Nuclear and Particle Physics* **2006**, *32*, DOI 10.1088/0954-3899/32/11/R01.

[23] O. Hen, G. A. Miller, et al., *Reviews of Modern Physics* **2017**, *89*, DOI 10.1103/RevModPhys.89.045002.

[24] A. Daniel, PhD thesis, **2007**.

[25] K. S. Egiyan, N. Dashyan, et al., **2003**, 1–11.

[26] L. B. Weinstein, E. Piasetzky, et al., *Nuclear Physics A* **2011**, *855*, 245–248.

[27] A. W. Thomas, *International Journal of Modern Physics E* **2018**, *27*, DOI 10.1142/S0218301318400013.

[28] W. K. Brooks, H. Hakobyan, et al., **2014**.